Pergamon

Int. J. Heat Mass Transfer. Vol. 38, No. 13, pp. 2427–2444, 1995
Copyright © 1995 Elsevier Science Ltd
Printed in Great Britain. All rights reserved
0017–9310/95 $9.50+0.00

0017–9310(94)00357–2

Heat transfer and flow structure in laminar and turbulent flows in a rectangular channel with longitudinal vortices

P. DEB, G. BISWAS
Department of Mechanical Engineering, Indian Institute of Technology, Kanpur 208016, India

and

N. K. MITRA†
Inst für Thermo-und Fluiddynamik, Ruhr University Bochum, 44780 Bochum, Germany

(*Received* 6 *June* 1994 *and in final form* 23 *November* 1994)

Abstract—Heat transfer characteristics and flow structure in laminar and turbulent flows through a rectangular channel containing built-in vortex generators have been analyzed by means of solutions of the full Navier–Stokes and energy equations. The geometrical configuration of interest is representative of single element of a plate-fin cross-flow heat exchanger. Each winglet-pair induces longitudinal vortices behind it. These vortices swirl the flow around the axis parallel to the mainstream direction and strongly enhance the exchange of fluid between the wall and the core region which causes high heat transfer augmentation. A detailed evaluation of the performance parameters in the laminar flow regime with regard to the enhancement of heat transfer using winglet-type vortex generators has been accomplished in this study. It may be mentioned that for some special applications the fluid velocity becomes very high and one may encounter turbulent flows in plate-fin heat exchangers. In the present study, the predictions for turbulent flows have been made and an effort has been undertaken to compare the accuracy of the predictive procedure with well documented experiments of another research group. The computational results agree reasonably well with their experimental counterpart.

INTRODUCTION

The subject of enhanced heat transfer is of serious interest in heat exchanger applications. Concepts like space and energy optimization in power and process industries call for more and more compact designs of heat exchangers. Specially designed surfaces use protrusions mounted on them to enhance heat transfer. Some typical examples of the enhanced heat transfer surfaces which are very popular in different industrial applications [1] are shown in Fig. 1. There have been a number of survey articles and handbook sections prepared that deal with the augmentation of heat transfer for different applications [2–4]. Special surface geometries bring about the transport-enhancement by establishing a higher heat transfer coefficient.

Protrusions can be mounted on the channel walls in order to generate longitudinal vortices which disrupt the growth of the boundary layer and thereby enhance the heat transfer between the flowing fluid and the channel walls. Two relevant applications using such flow configurations are the heat transfer between the gas and the fin in the case of gas–liquid fin-tube cross-flow heat exchangers and the heat transfer between the flowing fluid and plates in the case of plate-fin heat exchangers.

Experimental investigations due to Edwards and Alker [5], Russels *et al.* [6], Fiebig *et al.* [7, 8] and Tiggelbeck *et al.* [9] can be referred to in connection with augmentation of heat transfer by means of longitudinal vortices. Experimental investigation due to Fiebig *et al.* [8] is the first systematic study to compare the performance of different kinds of vortex generators, viz. namely delta wing, rectangular wing, delta winglet pair and rectangular winglet pair in the Reynolds number range of 1360 and 2270. Their observations depict that the delta wing is the best vortex generator from heat transfer point of view. Tiggelbeck *et al.* [9] use multiple rows of vortex generators in an aligned arrangement within a channel and observe their influence on flow structure. The flow structure in the wake of the second row is qualitatively similar to that of the first row. Their flow visualization by a laser light sheet technique has revealed that the concentrated vortex pair generated by a small aspect ratio delta wing at large angle of attack has an elliptic shape due to the influence of channel walls. They also observe that the peak value of the spanwise-averaged Nusselt number at the wake of the second row is strongly dependent on the spacing of the two rows.

---

† Author to whom correspondence should be addressed.

NOMENCLATURE

B	channel width
b	twice the winglet height
C_f	skin friction coefficient, $[2(\partial u/\partial y)_w]/(\rho U_{av}^2)$
$\bar{C}_f$	combined spanwise average skin friction coefficient
C_μ	empirical constant
E	function of wall roughness in the law of the wall
G	generation of turbulent kinetic energy
G_n	generation of turbulent kinetic energy (nondimensional)
H	channel height
h	local heat transfer coefficient, $-\mathrm{k}(\partial T/\partial y)_w/(T_w - T_b)$
I	turbulent intensity
k	thermal conductivity of the fluid
k	turbulent kinetic energy
k_n	$k/\bar{U}_o^2$, turbulent kinetic energy (nondimensional)
L	length of the channel
Nu	local Nusselt number based on bulk temperature of the fluid
$\overline{Nu}$	spanwise average Nusselt number
$\overline{Nu}_{sa}$	combined spanwise average Nusselt number for the channel
p	static pressure
P	nondimensional static pressure, $p/\rho U_0^2$
P_{fn}	Pee function
Pr	Prandtl number, $\mu c_p/\mathrm{k}$
q	wall heat flux
q_w	wall heat flux for turbulent flow
$q_{w,n}$	wall heat flux for turbulent flow (nondimensional)
Re	$U_o H/\nu$
$Re_{H/2}$	$U_0 H/2\nu$
S	twice the wing area
T	temperature
t	nondimensional time
U, V, W	axial, vertical, spanwise components of laminar velocity (nondimensional)
$\bar{U}, \bar{V}, \bar{W}$	axial, vertical, spanwise components of time-mean velocity (nondimensional)
u, v, w	axial, vertical, spanwise components of velocity
$\bar{u}, \bar{v}, \bar{w}$,	axial, vertical, spanwise components of time-mean fluctuating velocity
u', v', w'	axial, vertical, spanwise components of fluctuating velocity
u_τ	$\sqrt{(\tau_w/\rho)}$, friction velocity
$u_{\tau,n}$	$\sqrt{(\tau_{w,n})}$, friction velocity (nondimensional), $C_\mu^{1/4}k_n^{1/2}$
X, Y, Z	axial, vertical or normal, and spanwise coordinates (normalized by H)
x, y, z	axial, vertical or normal, and spanwise dimension of coordinates
Y^+	yu_τ/ν or $Y\,Reu_{\tau,n}$, nondimensional distance from the wall in the law of the wall.

Greek symbols

α	aspect ratio of the channel, B/H
$\alpha_{t,n}$	eddy diffusivity (nondimensional)
β	angle of attack of the vortex generator
θ	temperature (nondimensional), $(T - T_\infty)/(T_w - T_\infty)$
$\bar{\theta}$	time-mean temperature component (nondimensional)
ε	dissipation rate of turbulent kinetic energy
ε_n	$\varepsilon/(\bar{U}_o^3/H)$, dissipation rate of turbulent kinetic energy (nondimensional)
$\bar{\varepsilon}_n$	average dissipation rate of turbulent kinetic energy (nondimensional)
χ	von Karman constant and equal to 0.42
Λ	aspect ratio of the obstacle
λ	a constant and equal to 0.09
ν	kinematic viscosity of the fluid
ν_t	$C_\mu k^2/\varepsilon$, turbulent kinematic viscosity
$\nu_{t,n}$	$C_\mu Re k_n^2/\varepsilon_n$, turbulent kinematic viscosity (nondimensional)
ρ	density of the fluid
τ_w	wall shear stress
$\tau_{w,n}$	wall shear stress (nondimensional)
$\tau_{w,n}^x$	x-component of wall shear stress (nondimensional)
$\tau_{w,n}^z$	z-component of wall shear stress (nondimensional).

Subscripts

w	wall
b	bulk condition
av	average velocity at the inlet of the channel
1	bottom fin-plate
2	top fin-plate
sa	spanwise combination of top and bottom plate
o	condition in the free-stream
p	corresponding to grid point adjacent to the the wall.

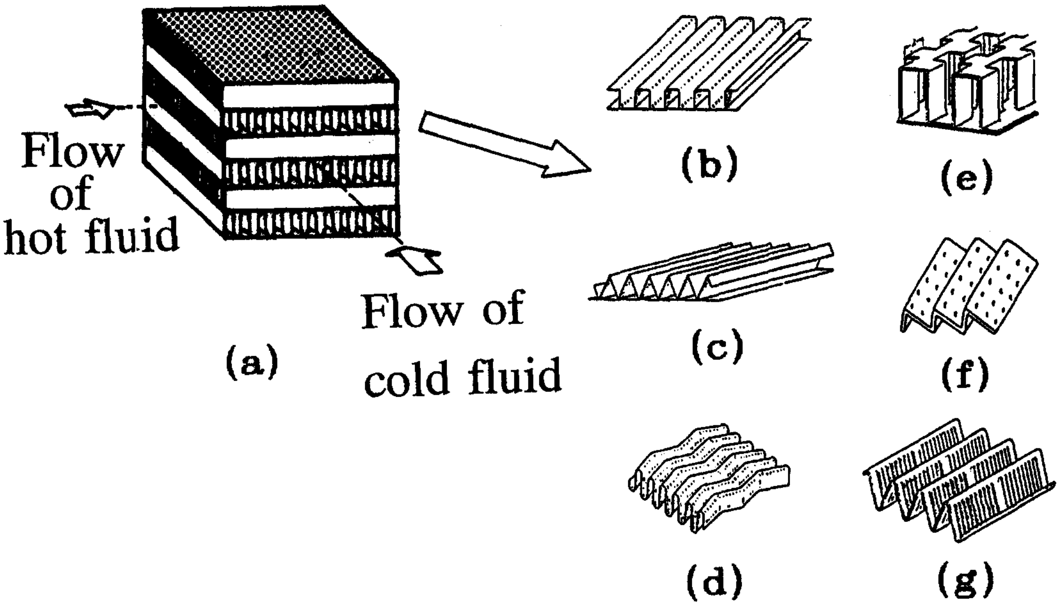

Fig. 1. (a) Plate-fin heat exchanger and its surface geometries; (b) plain rectangular fins; (c) plain triangular fins; (d) wavy fins; (e) offset strip fins; (f) perforated fins and (g) louvered fins; after Webb [1].

Computational studies on related topics have been performed by Fiebig *et al.* [10] and Biswas and Chattopadhyay [11] for laminar flows in a geometrical configuration of delta wing placed inside a channel. Both studies have discussed the influence of angle of attack and Reynolds number on velocity and temperature fields.

Recently, Dong [12] and Valencia [13] have conducted experimental investigations to observe the influence of winglet-type vortex generators in a channel with a built-in circular tube. Biswas *et al.* [14] have observed that in the absence of the winglet-type vortex generators, relatively little heat transfer takes place in the downstream of the circular tube which is a recirculation region with low velocity fluid. However, they observe an enhancement of heat transfer as high as 240% in the wake region behind the cylinder in the presence of winglet-type longitudinal vortex generators.

Many researchers have observed longitudinal vortices in various complex flow configurations. Naturally, the interaction of such vortices with boundary layer and its effect on heat transfer is a subject of interest to them. Some examples are Taylor–Görtler vortices in boundary layers on concave curved surfaces, horseshoe vortices formed by an obstruction protruding from a surface and wingtip vortices impinging on a downstream surface. The embedded vortex is capable of strongly perturbing the boundary layer thickness and influencing the heat transfer characteristics. In addition, longitudinal vortices usually maintain their coherence over a long streamwise distance. As a consequence, the heat transfer effects behind a vortex generator are very persistent. Eibeck and Eaton [15], Westphal and Mehta [16] have worked extensively in this field with more focus to the turbulent boundary layer. Eibeck and Eaton [15] have conducted experiments on longitudinal vortices embedded in a turbulent boundary layer and resultant heat transfer effects. Longitudinal vortices are found to influence the heat transfer behaviour significantly. Local Stanton number is increased by as much as 24% resulting in a net increase in spanwise average heat transfer coefficient. Despite the presence of turbulent diffusion, the influence of longitudinal vortices on momentum and energy transport can be traced at a location as far downstream as 60 wing chords behind the delta wing. Recently Zhu *et al.* [17] have investigated the influence of four types of longitudinal vortex generators (delta wing, rectangular wing, delta winglet pair and rectangular winglet pair) on heat transfer and flow loss in turbulent channel flows.

In the present paper, a numerical investigation has been undertaken to predict the laminar and turbulent flows and associated temperature fields in channels with delta winglet-type vortex generators. The present investigation has the following purposes:

(i) Validation of the turbulent flow model through comparison with experiment of Pauley and Eaton [18, 19] and Eaton [20].

(ii) Prediction of the heat transfer and flow losses in the configuration of interest. We envisage to predict the distribution of spanwise-average-Nusselt number and the distribution of spanwise-average-skin friction coefficient on the walls of a channel with built-in vortex generators.

STATEMENT OF THE PROBLEM

As it has been stated above, computation is performed in a channel which is formed by two neigh-

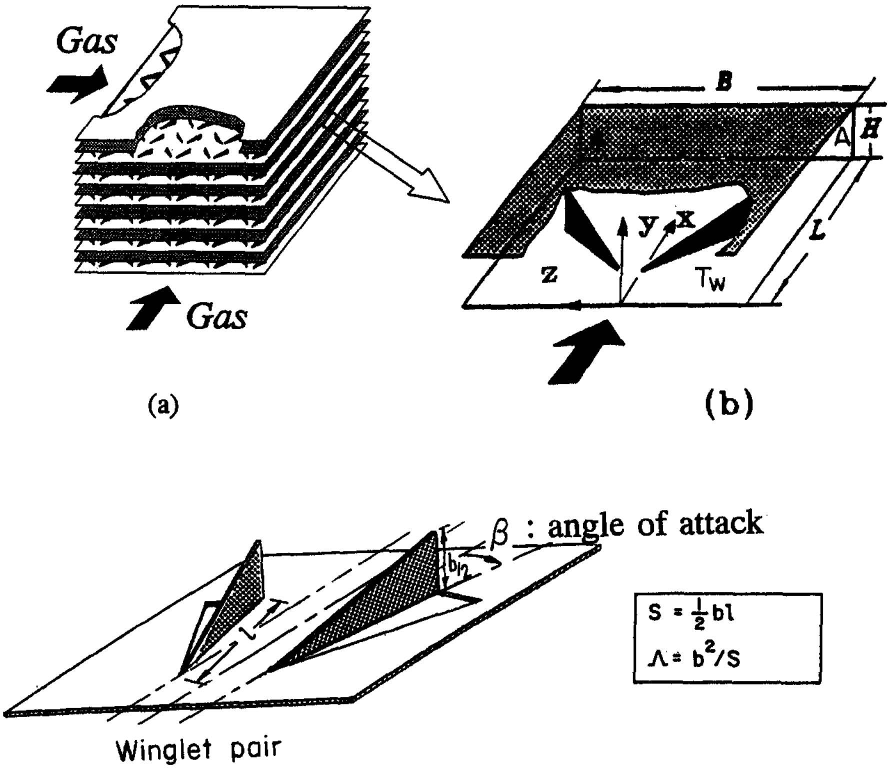

Fig. 2. (a) Proposed surface geometry that uses delta winglets. (b) Computational model.

boring fins (Fig. 2). The obstacle in the form of a winglet-pair (of zero thickness) is placed inside the channel. One side of each winglet-pair is fixed on the bottom wall and the trailing edge of each is free. Since symmetry prevails in the central vertical plane of the channel, the flow field in only half of the channel is computed. In the present study, the numerical simulations deal with two different regimes of flow, viz., namely laminar and turbulent. In the subsequent section, the governing conservation equations for laminar and turbulent flows and the appropriate boundary conditions will be discussed.

GOVERNING EQUATIONS

The time averaged Navier–Stokes equations for turbulent incompressible flow where the Reynolds stresses are expressed via the eddy-viscosity concept have been used as governing equations. These equations are written in a Cartesian tensor form as

$$\frac{\partial \bar{U}_j}{\partial X_j} = 0 \tag{1}$$

$$\frac{\mathrm{D}\bar{U}_j}{\mathrm{D}t} = -\frac{\partial(\mathrm{P}+2k_\mathrm{n}/3)}{\partial X_j} + \frac{1}{Re}\frac{\partial}{\partial X_i}\left[(1+\nu_{\mathrm{t,n}})\left(\frac{\partial \bar{U}_i}{\partial X_j}+\frac{\partial \bar{U}_j}{\partial X_i}\right)\right] \tag{2}$$

$$\frac{\mathrm{D}\bar{\theta}}{\mathrm{D}t} = \frac{1}{RePr}\frac{\partial}{\partial X_i}\left[(1+\alpha_{\mathrm{t,n}})\frac{\partial \bar{\theta}}{\partial X_i}\right] \tag{3}$$

where $\bar{U}_j$ and $\bar{\theta}$ are nondimensional time-mean velocity components and temperature, $\nu_{\mathrm{t,n}}$ is the nondimensional kinematic viscosity, $\alpha_{\mathrm{t,n}}$ is the nondimensional eddy diffusivity and k_n is the nondimensional kinetic energy of turbulence. The subscripts i and j can take the values 1, 2 or 3 in the three coordinate directions X_1, X_2 and X_3, respectively. The X_1, X_2 and X_3 are equivalent to X, Y and Z in Cartesian coordinates. The Reynolds number Re is defined on the basis of average axial velocity at the inlet and the laminar viscosity as $Re = \bar{U}_0 H/\nu$. The Prandtl number of the fluid is denoted by Pr.

The turbulent kinematic viscosity $\nu_{\mathrm{t,n}}$ is given by

$$\nu_{\mathrm{t,n}} = C_\mu Re\, k_\mathrm{n}^2/\varepsilon_\mathrm{n}. \tag{4}$$

In the above equation C_μ is a constant (equal to 0.09) and ε_n is the dissipation rate of turbulent kinetic energy (normalized with respect to $\bar{U}_0^3/H$). The nondimensional eddy diffusivity $\alpha_{\mathrm{t,n}}$ is given by

$$\alpha_{\mathrm{t,n}} = C_\mu RePrk_\mathrm{n}^2/(\sigma_\mathrm{t}\varepsilon_\mathrm{n}) \tag{5}$$

where σ_t is the turbulent Prandtl number. Generally, $\sigma_\mathrm{t} = 0.9$. The modeled transport equations for k_n and ε_n are

$$\frac{\mathrm{D}k_n}{\mathrm{D}t} = \frac{1}{Re}\frac{\partial}{\partial X_i}\left[\frac{\nu_{t,n}}{\sigma_k}\frac{\partial k_n}{\partial X_i}\right] + G_n - \varepsilon_n \tag{6}$$

$$\frac{\mathrm{D}\varepsilon_n}{\mathrm{D}t} = \frac{1}{Re}\frac{\partial}{\partial X_i}\left[\frac{\nu_{t,n}}{\sigma_\varepsilon}\frac{\partial \varepsilon_n}{\partial X_i}\right] + C_1\varepsilon_n G_n/k_n - C_2\varepsilon_n^2/k_n. \tag{7}$$

Here, G_n is the generation of turbulent kinetic energy (nondimensional) given by

$$G_n = \frac{(1+\nu_{t,n})}{Re}\left(\frac{\partial \bar{U}_i}{\partial X_j} + \frac{\partial \bar{U}_j}{\partial X_i}\right)\frac{\partial \bar{U}_i}{\partial X_j} \tag{8}$$

and σ_k, σ_ε, C_1, C_2 are empirical constants: $\sigma_k = 1.0$, $\sigma_\varepsilon = 1.3$, $C_1 = 1.44$, $C_2 = 1.92$. These are based on wide range of experimental data. The argument for choosing these values are given in Launder and Spalding [21]. It may be mentioned that for the laminar flow computations, $\nu_{t,n}$ and k_n in equation (2) and $\alpha_{t,n}$ in equation (3) are taken as zero. Possibly, it is needless to say that for the laminar flows, the barred quantities should be read as unbarred variables.

BOUNDARY CONDITIONS FOR TURBULENT FLOW

The inlet conditions for velocity and temperature can be specified using the profiles we want to use. The turbulent kinetic energy k_n and its dissipation rate are calculated from the value of turbulent intensity specified at the inlet.

The inlet boundary conditions can be specified as follows:

$$\left.\begin{aligned} \bar{U}(Y) &= (u_{\tau,n}\ln(EY^+))/\chi \\ V &= 0 \\ W &= 0 \\ k_n &= 1.5I^2 \\ \varepsilon_n(Y) &= (k_n^{3/2}C_\mu^{3/4})/\chi^{Y} \quad \text{for} \quad Y < (\lambda/\chi) \\ &= (k_n^{3/2}C_\mu^{3/4})/\lambda \quad \text{for} \quad Y > (\lambda/\chi) \end{aligned}\right\} \tag{9}$$

where $u_{\tau,n}$ is nondimensional friction velocity, Y^+ is given by yu_τ/ν, I is turbulent intensity, $\chi = 0.42$ which is known as von Karman constant, λ is a constant prescribing ramp distribution of mixing length in boundary layers and equal to 0.09 and $E = 9.0$. The boundary conditions for the outlet and the confining walls (both no-slip and free-slip) as shown in Fig. 3 are treated as follows:

outlet

$$\frac{\partial f}{\partial X} = 0 \quad f = \{\bar{U}, \bar{V}, \bar{W}, \bar{\theta}, k_n, \varepsilon_n\} \tag{10}$$

free-slip (symmetric) wall (plane I, III)

$$\bar{W} = 0 \quad \frac{\partial f}{\partial Z} = 0 \quad f = \{\bar{U}, \bar{V}, \bar{\theta}, k_n, \varepsilon_n\} \tag{11}$$

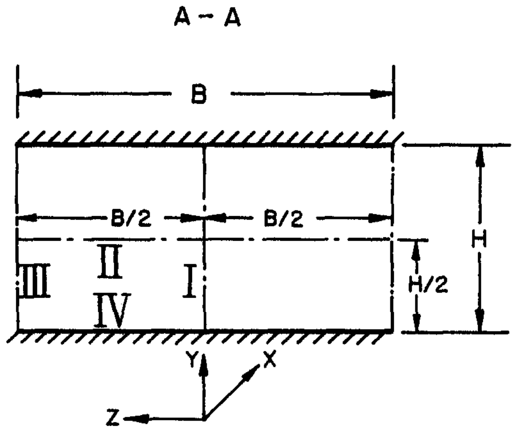

Fig. 3. Cross-section of the computational domain (A–A).

free-slip wall (plane II)

$$\bar{V} = 0, \quad \frac{\partial f}{\partial Y} = 0; \quad f = \{\bar{U}, \bar{W}, \bar{\theta}, k_n, \varepsilon_n\} \tag{12}$$

no-slip wall (plane IV)

$$\bar{U} = \bar{V} = \bar{W} = 0, \quad \bar{\theta} = 1. \tag{13}$$

The wall functions due to Launder and Spalding [21] are used to bridge the near wall region:

$$\tau^x_{w,n} = \frac{\bar{U}_p C_\mu^{1/4} k_{n,p}^{1/2}\chi}{\ln(EY_p^+)} \tag{14}$$

$$\tau^z_{w,n} = \frac{\bar{W}_p C_\mu^{1/4} k_{n,p}^{1/2}\chi}{\ln(EY_p^+)} \tag{15}$$

where $Y_p^+ = Y_p Re\, C_\mu^{1/4} k_{n,p}^{1/2}$. The subscript p refers to the first grid point adjacent to the wall. The production rate of k_n and the average dissipation rate of $\bar{\varepsilon}_n$ over a near wall cell for the equation (6) at point p are computed from the following:

$$G_{n,p} = \sqrt{((\tau^x_{w,n})^2 + (\tau^z_{w,n})^2)}\sqrt{(\bar{U}_p^2 + \bar{W}_p^2)}/Y_p \tag{16}$$

$$\bar{\varepsilon}_{n,p} = \frac{1}{Y^p}\int_0^{Y_p} \varepsilon\,\mathrm{d}Y = \frac{C_\mu^{3/4} k_{n,p}^{3/2}}{\chi Y_p}\ln(EY_p^+). \tag{17}$$

Instead of using equation (7) near the wall, the ε_n at point p is computed from

$$\varepsilon_{n,p} = \frac{C_\mu^{3/4} k_{n,p}^{3/2}}{\chi Y_p}. \tag{18}$$

In order to calculate the wall functions for temperature, the heat flux at the near wall point can be expressed in the following way:

$$q_{w,n} = \frac{(\bar{\theta}_w - \bar{\theta}) C_\mu^{1/4} k_{n,p}^{1/2}}{(\sigma_t \ln(EY_p^+)/\chi) + P_{fn}} \tag{19}$$

where $q_{w,n}$ is the nondimensional heat flux at the wall given by

$$q_{w,n} = \frac{q_w}{\rho c_p U_0 (T_w - T_\infty)}. \tag{20}$$

It may be mentioned that P_{fn} in equation (19) is the Pee function which may be written as (see Dutta and Acharya [22])

$$P_{\mathrm{fn}} = 9\left[\frac{Pr}{\sigma_t} - 1\right]\left[\frac{Pr}{\sigma_t}\right]^{-1/4}. \tag{21}$$

BOUNDARY CONDITIONS FOR LAMINAR FLOW

For the laminar flow, the boundary conditions of interest in this investigation are:

Top and bottom plates

$$U = V = W = 0 \quad \theta = 1 \tag{22}$$

Side wall ($z = B/2$) and midplane ($z = 0$)

$$W = \left(\frac{\partial V}{\partial Z}\right) = \left(\frac{\partial U}{\partial Z}\right) = 0 \quad \left(\frac{\partial \theta}{\partial Z}\right) = 0 \tag{23}$$

At the channel inlet

$$U = U(Y), \quad V = W = 0 \quad \theta = 0. \tag{24}$$

At the exit, a smooth transition through the outflow boundary is ensured by setting:

$$\frac{\partial^2 U}{\partial X^2} = \frac{\partial^2 V}{\partial X^2} = \frac{\partial^2 W}{\partial X^2} = 0 \quad \frac{\partial^2 \theta}{\partial X^2} = 0. \tag{25}$$

No-slip boundary conditions for the velocities on the obstacle are used. The temperature of the obstacle is considered constant and equal to T_ω.

METHOD OF SOLUTION

Computational domain is divided into a set of rectangular cells and a staggered grid arrangement is used such that the velocity components are defined at the center of the cell faces to which they are normal. The pressure and temperature are defined at the center of the cell.

A modified version of Marker and Cell (MAC) method due to Harlow and Welch [23] and Hirt and Cook [24] is used to obtain the numerical solution of the governing equations.

Convective terms of the momentum equations are discretized using a weighted average of second upwind and space centered scheme (Hirt *et al.* [25]). Diffusive terms are discretized by a central difference scheme.

In the MAC algorithm, the velocities for the next time step are calculated explicitly using the convective accelerations, viscous diffusions and pressure gradients at the previous time level. The explicitly advanced velocities may not necessarily lead to a flow field with zero mass divergence in each cell. This implies that at this stage the pressure distribution is not correct. Pressure in each cell is corrected in such a way that there is no net mass flow in or out of the cell.

After evaluating the correct velocities, the energy equation is solved with an Successive Over-Relaxation technique to determine the temperature field.

SOME IMPROVEMENTS ON DISCRETIZATION OF CONVECTIVE TERMS

More accurate solutions can be obtained if the convective terms are discretized by higher order schemes. Davis and Moore [26] use the MAC method with a multidimensional third-order upwinding scheme. Needless to mention that their marching algorithm for the momentum equation is explicit and the stability restriction concerning the CFL condition $[(U\delta t/\delta X) \leqslant 1,\ (V\delta t/\delta Y) \leqslant 1$ and $(W\delta t/\delta Z) \leqslant 1]$ is satisfied. The multidimensional third-order upwinding is in principle similar to the one-dimensional quadratic upstream interpolation scheme of Leonard [27].

We have combined the QUICK scheme of Leonard [27] and a upwind scheme in order to improve the accuracy of discretized convective terms of the governing equations. For an example, the discretization of the term $\partial(uv)/\partial y$ for the x-momentum equation has been accomplished in the following way:

$$\left[\frac{\partial(UV)}{\partial Y}\right] = (1-\alpha_y)\left[\frac{\partial(UV)}{\partial Y}\right]_{\mathrm{quick}} + \alpha_y\left[\frac{\partial(UV)}{\partial Y}\right]_{\mathrm{up}} \tag{26}$$

where α_y is contribution of the upwind factor. The factor α_y can be found from the following calculation:

$$\alpha_y = \frac{Re_\Delta^{\mathrm{c}} - Re_\Delta^{\min}}{Re_\Delta^{\max} - Re_\Delta^{\min}} \tag{27}$$

where

$Re_\Delta^{\min}$ (minimum cell Reynolds number)

$$= \min\left[\left|\frac{U\delta X}{v}\right|,\ \left|\frac{V\delta Y}{v}\right|,\ \left|\frac{W\delta Z}{v}\right|\right]$$

$Re_\Delta^{\max}$ (maximum cell Reynolds number)

$$= \max\left[\left|\frac{U\delta X}{v}\right|,\ \left|\frac{V\delta Y}{v}\right|,\ \left|\frac{W\delta Z}{v}\right|\right]$$

Re_Δ^{c} = calculated cell Reynolds number of any cell.

The third-order upwind scheme of Kawamura *et al.* [28] and Shirayama [29] is represented by blending the fourth-order central difference of the first derivative and the fourth-order dissipation term. However, an attempt has been made to use the third order upwinding scheme in the present investigation. Three different discretization schemes, as mentioned above, are tested on a model problem of flow in a lid-driven square cavity.

In Fig. 4, u velocity components at the vertical mid plane of the square cavity for a Reynolds number of 400 are plotted. A (42 × 42) grid is used and the results due to three different discretization schemes are compared with the results obtained by Ghia *et al.* [30]. It may be mentioned that Ghia *et al.* have employed a 129 × 129 grid via a multigrid technique. Figure 4 shows reasonably good agreement between Ghia *et al.*'s result and all the three cases of present computation. The v velocity components at the horizontal

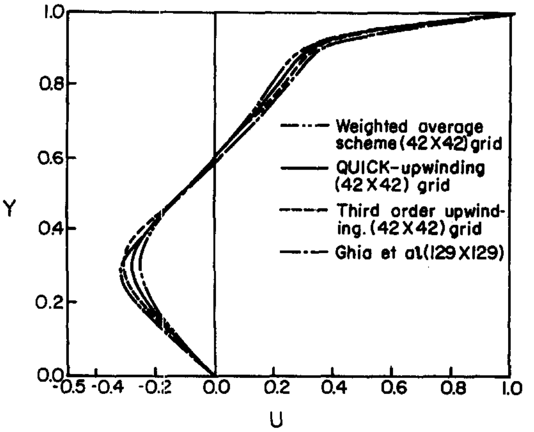

Fig. 4. Variation of U velocity along the vertical midplane for the lid-driven flow in a square cavity.

mid plane for the same Reynolds number ($Re = 400$) are shown in Fig. 5. It is evident that the results obtained due to all the three schemes demonstrate reasonably good agreement with the results due to Ghia *et al.* [30].

It has also been observed that the weighted average scheme takes considerably less CPU time to compute. The computational accuracy of the weighted average scheme is also calibrated by comparing the peripheral average local Nusselt numbers predicted by our numerical scheme with those of available literature (Shah and London [31]) for thermally developing and hydrodynamically developed flow through parallel plates. The results are found to be within about 3% for a Reynolds number of 500 and uniform wall temperature boundary condition. The turbulent flows have been computed by making use of QUICK-upwinding scheme. For laminar flows, weighted average scheme has been found to be time optimized and reasonably accurate.

An effort is undertaken to obtain grid independent results. For $Re = 500$ and $Pr = 0.7$, in a channel ($\alpha = 2$) with a built-in delta wing ($\Lambda = 1$) at an angle of attack (β) of 26°, reasonable agreement between the results obtained for 15×26 and 20×30 cross-stream grids is found. In the foregoing specification of cross-stream grids, 15 and 20 refer to the number of grids in the y direction. Similarly, 26 and 30 refer to the number of grids in the z direction. It may be mentioned that for a 15×26 cross-stream grid, 60 grid nodes are taken in the x direction for a nondimensional length of 8.4.

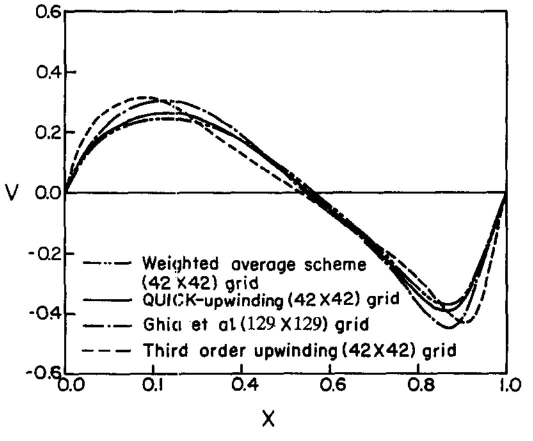

Fig. 5. Variation of V velocity along the horizontal midplane for the lid-driven flow in a square cavity.

Computations are also performed for a shorter channel of nondimensional length 4.3 for three different grids. Other geometrical and flow parameters concerning these computations remain the same as the earlier one. Computations for grids $30 \times 10 \times 13$, $30 \times 15 \times 26$ and $30 \times 30 \times 52$ have been carried out. The grids are specified in x, y and z directions, respectively. However, the extrapolated grid-independent average Nusselt number differs from the corresponding Nusselt number obtained with the coarsest grid by less than 10%. A grid size of $30 \times 15 \times 26$ produces average Nusselt number which differs from this extrapolated grid-independent average Nusselt number by less than 3%. Hence most of the computations are done by using a 15×26 cross-stream grids. In some cases, cross-stream grids finer than (15×26) are used for special requirements, namely accommodating some typical obstacle position and obtaining a closer point near the wall in the case of turbulent flow computations. The grids in the streamwise directions are suitably chosen to cover the required length of the channel with a reasonably good accuracy.

In the problem of a channel with a built-in winglet-pair, for a grid size of $60 \times 15 \times 26$ (in x, y and z directions, respectively) and Reynolds number of 1000 (laminar flow) the CPU time with respect to steady solution is 157 min.

For a Reynolds number of 15000 (turbulent flow), in a shorter channel of non-dimensional length 4.3, the corresponding CPU time with respect to steady solution is 620 min and the grid size is $30 \times 15 \times 27$.

The laminar flow computations are performed on a HP-9000/850 series computer whereas the computations for the turbulent flows are performed on a CONVEX C-220 computer.

PERFORMANCE OF DELTA WINGLET-PAIR TYPE VORTEX GENERATORS FOR LAMINAR FLOWS

A number of computations have been performed with a delta winglet-pair as vortex generators in the channel. Air has been chosen as the working fluid, hence the Prandtl number of all these studies is 0.7.

Figure 6 shows cross-stream velocity vectors at various axial locations of the channel with a built-in winglet-pair. In order to have a lucid understanding of the structure secondary flow, various magnified scales for the average axial velocity have been used for different cross-stream planes.

Normalized streamwise vorticity contours for the above mentioned case have been shown in Fig. 7. The

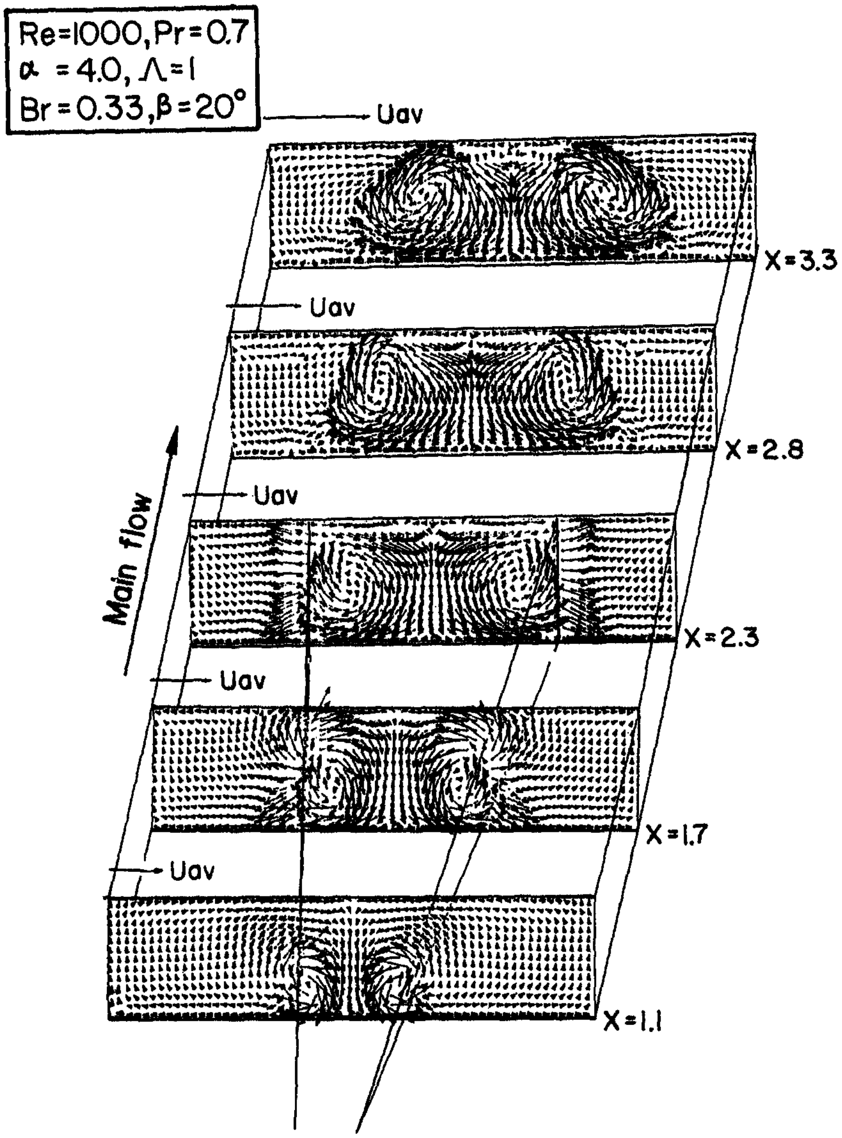

Fig. 6. Cross-stream velocity vectors at different axial locations behind the winglet-pair in a channel.

dotted lines indicate negative vorticity. Peak vorticity occurs in the vortex centers and near the symmetry sides (side walls) where the symmetry boundary conditions lead to rapid change in the direction of flow of the secondary vortices.

In order to appreciate the heat transfer performance of the vortex generators, the combined spanwise average Nusselt number

$$\overline{Nu}_{sa} = \frac{B(q_1+q_2)(H/k)}{2\int_0^{B/2}(T_{w1}(x,z)-T_b(x))\,dz+2\int_0^{B/2}(T_{w2}(x,z)-T_b(x))\,dz} \qquad (28)$$

has been calculated at each longitudinal location. Figure 8 shows the effect of winglet-pair on distribution of $\overline{Nu}_{sa}$ in a channel for various Reynolds numbers. Winglets with higher Reynolds number induce higher vortex strength and thereby higher heat transfer is brought about. For all the Reynolds numbers, the $\overline{Nu}_{sa}$ distribution has been compared with the corresponding plane channel value. At a nondimensional distance of 2.5 from the inlet, for a Reynolds number of 2000, we observe an enhancement of 30% in the $\overline{Nu}_{sa}$ over the corresponding value for a channel without any obstacle.

The combined spanwise average friction coefficient in the channel has been defined as

$$\bar{C}_f = \frac{\mu\left[2\int_0^{B/2}\left(\frac{\partial u}{\partial y}\right)_{y=0}dz+2\int_0^{B/2}\left(\frac{\partial u}{\partial y}\right)_{y=H}dz\right]}{\frac{\rho}{2}U_{av}^2(2B)} \qquad (29)$$

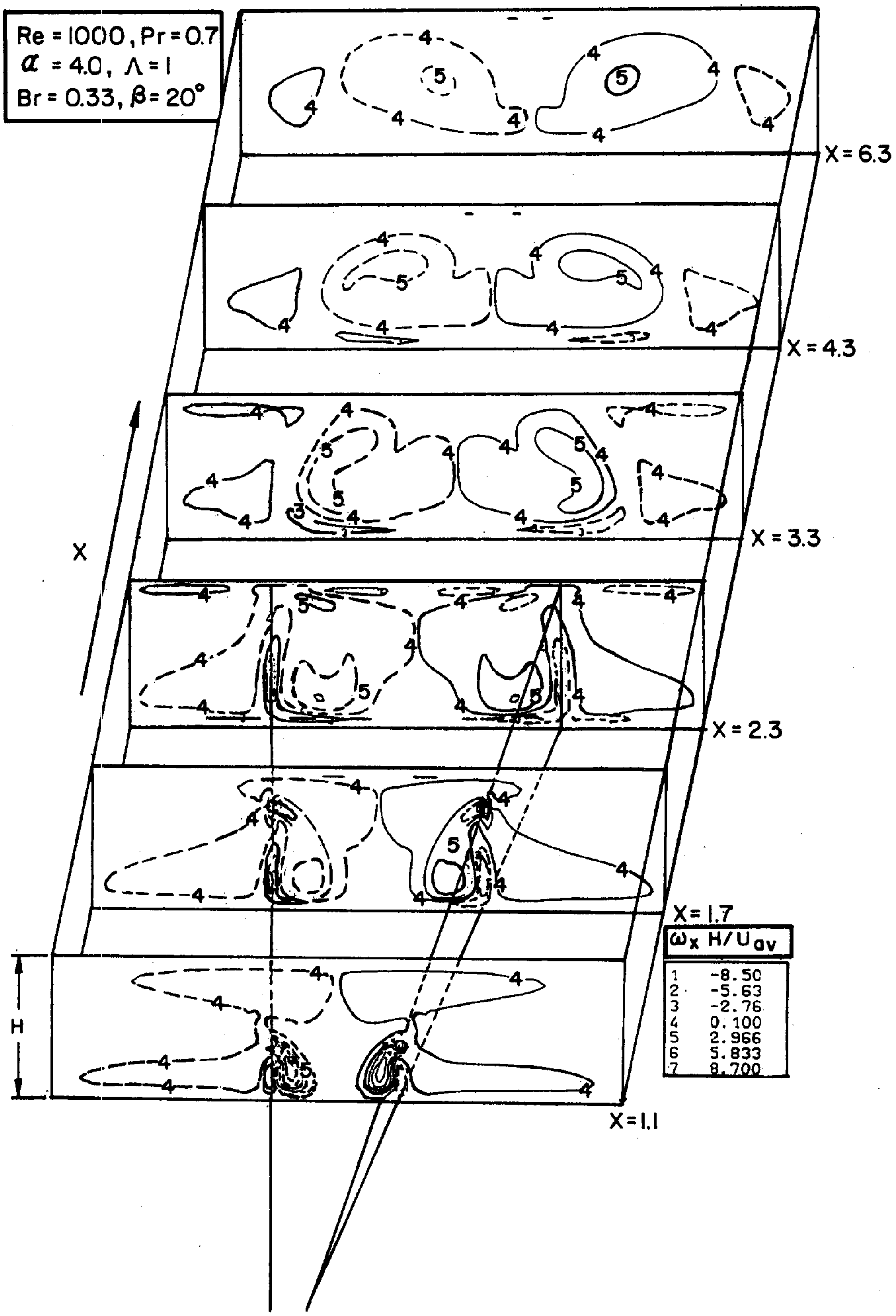

Fig. 7. Contours of normalized streamwise vorticity in the channel.

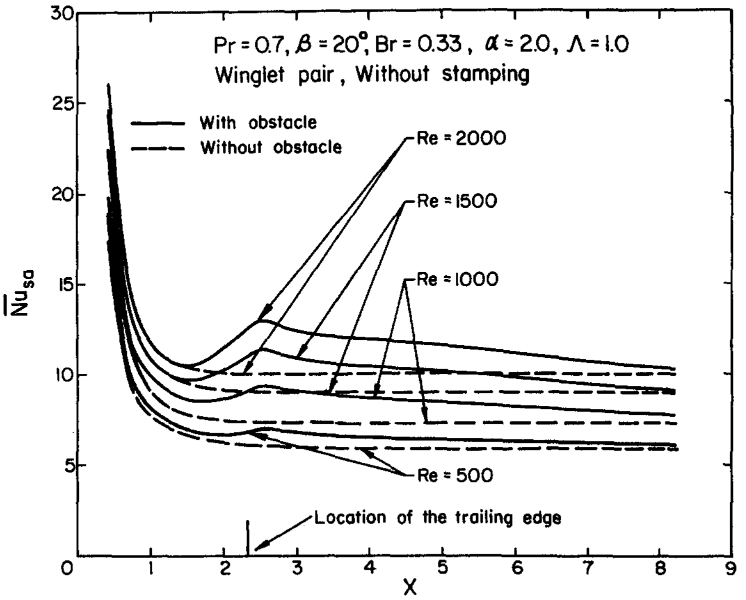

Fig. 8. Effect of winglet-pair on combined-spanwise-average Nusselt number distribution in the channel for different Reynolds numbers.

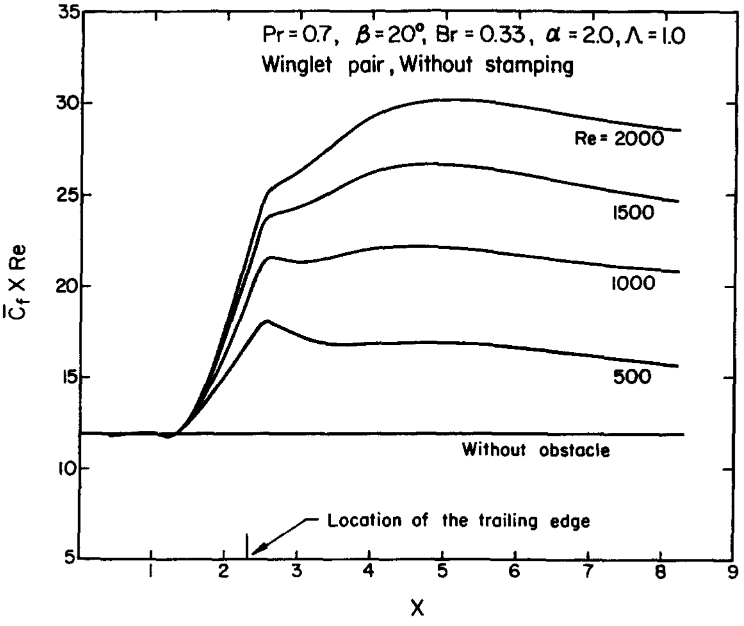

Fig. 9. Effect of Reynolds number on the distribution of combined spanwise-average-skin-friction in the channel with built-in winglet-pair.

and the parameter ($\bar{C}_f \times Re$) has been evaluated to predict the performance of the vortex generators. Effect of Reynolds number on the distribution of ($\bar{C}_f \times Re$) for the built-in winglet-pair has been shown in Fig. 9. Increasing ($\bar{C}_f \times Re$) for higher Reynolds number is a consequence of increased vortex strength for higher flow velocities. For Reynolds number of 2000, the ($\bar{C}_f \times Re$) is 82% more than that of Reynolds number of 500 at the exit of the channel.

TURBULENT FLOW AND HEAT TRANSFER

It may be mentioned that the study of laminar flow in the present work is not for computational simplification. Usually, the fin spacing is so small and the mean velocity range is such that the flows are often laminar (Kakac *et al.* [32]). However, for some special applications, the velocity becomes such that one may encounter turbulent flows in plate-fin type heat

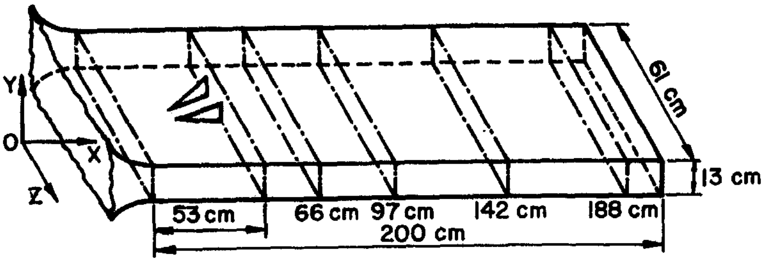

Fig. 10. Schematic of the experimental facility of Pauley and Eaton [18, 19].

exchangers. Therefore, a detailed analysis of turbulent flow in an element of such heat exchangers is necessary.

COMPARISON OF NUMERICAL AND EXPERIMENTAL RESULTS

Experimental data for three-dimensional turbulent flows in a rectangular channel containing longitudinal vortex pairs have been presented in Pauley and Eaton [18, 19] and Eaton [20]. Figure 10 shows the schematic of the experimental facility. This facility has a 200 cm long test section with a 13 cm × 61 cm cross-section and is operated at a normal free-stream velocity of $U_0 = 16\ \mathrm{m\ s^{-1}}$. A pair of delta winglets is used as vortex generators and is located at 53 cm downstream from the inlet. The angles of attack of the vortex generators can be varied. The case with the winglet height of 2 cm and a length of 5 cm with 18° angle of attack, which has been referred to in Pauley and Eaton [18, 19] and Eaton [20], is chosen for the present simulation. Pauley and Eaton [18, 19] and Eaton [20] have conducted measurement at four cross-sections, namely, $x = 66, 97, 142$ and 188 cm (see Fig. 10). The section $x = 97$ cm is selected as inlet of the computational domain used for the comparison. No experimental data is available for the turbulent variables at the axial station of $x = 66$ cm. The computational domain ends at the exit of the channel (i.e. at $x = 200$ cm). The measured data of Pauley and Eaton [19] for u, v, w, k and ε at the cross-section $x = 97$ cm are deployed as inlet profiles of these variables for the computational domain.

The flow is simulated for a Reynolds number of $Re_{H/2} = 67\ 000$, based on half height of the channel. Air has been used as a working fluid; hence Prandtl number of all computations is 0.7.

The comparison of secondary velocity vectors at three different planes in the channel can be observed through Fig. 11. A reasonably good agreement is confirmed between the experimental data and computed results. Both in the experiment and in the computation, the vortex transport and decay in the strength of secondary flow in various cross-sections are discerned.

Figure 12(a) shows the experimental values of isolines for the turbulent kinetic energy at two different cross-sections in the channel. In the downwash region, the boundary layer is thinned by the main vortex and the location for the peak value of turbulent kinetic energy comes closer to the wall. In the upwash region, the iso-kinetic energy lines are more uniformly placed. Although the k–ε model formally employs some restrictive assumptions, the results obtained from the present computation shown in Fig. 12(b) seem to match surprisingly with the experiments.

An engineering computation of turbulent flow concerns determination of mean axial velocity profiles in a flow field and the effect of time-dependent fluctuations on them. Figures 13 compares the experimental and computed axial velocity profiles (normalized) at a particular axial distance for five spanwise locations. In Fig. 13, the five spanwise locations at $z = 2.4, 4.3, 6.2, 8.1$ and 10.0 cm represent the central core region (A), down wash region (B), region of vortex core (C), upwash region (D) and outer vortex region (E) of the cross-section at $x = 142$ cm.

In the central region (A) of the cross-section at $x = 142$ cm where the boundary layer is thinned significantly by the influence of strong downflow (refer to Fig. 11), the velocity profile shows a usual two dimensional distribution. However, in this region the agreement between the computational and experimental results is indeed good. In the upwash region (D) the streamwise velocity profile is not so correctly reproduced by the simulation. The departure of prediction from the experimental result goes up to 6%. In other regions of the cross-section at $x = 142$ cm, a reasonably good agreement between the experimental results and the prediction is observed.

Figure 14 compares the computed and measured values of turbulent kinetic energy distribution in the y-direction for different z locations at an axial station of $x = 188$ cm. In some cases, (at $z = 6.2$ cm), the computed results overpredict the results of Eaton [20]. By and large, the comparison implicates acceptable agreement between the prediction and the computed results.

PREDICTION OF PERTINENT PERFORMANCE PARAMETERS FOR TURBULENT FLOWS

For the turbulent flows the transport rate for momentum is high and the vortex generators are rather small in size with a view not to enhance much pressure penalty. Hence the height ($b/2$) of the wing-

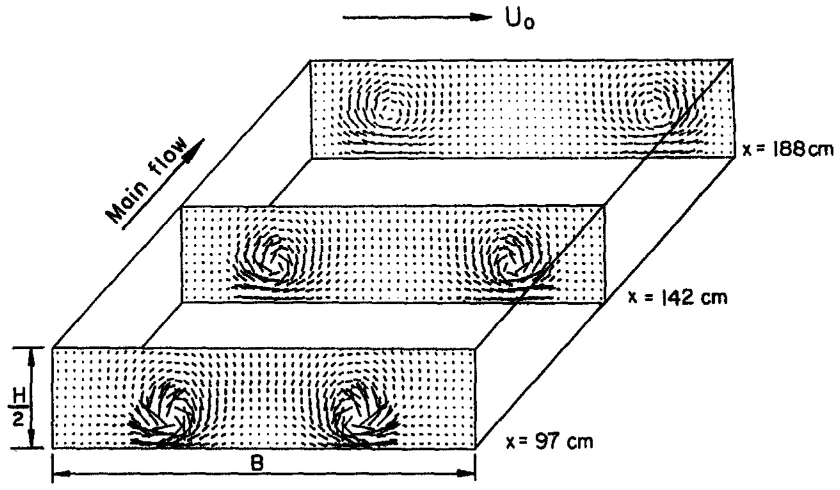

(a) Experiment due to Pauley and Eaton (1988 a, b)

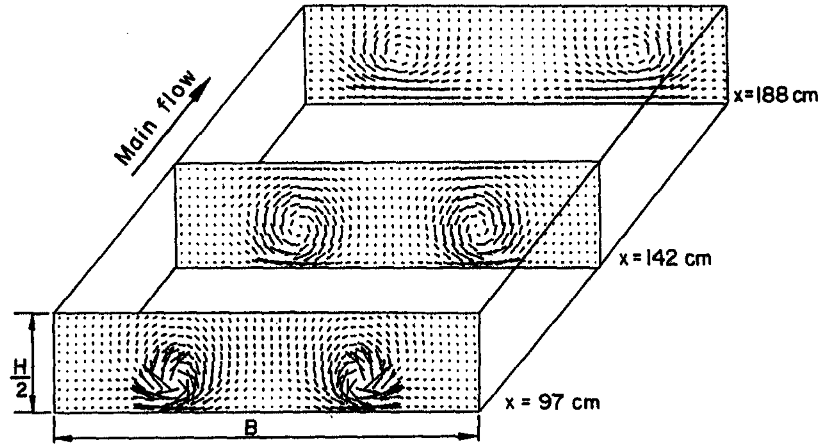

(b) Present computation

Fig. 11. Vector plots of secondary flow: $Re_{H/2} = 67\,000$.

lets for such computations is very small compared to the channel height ($b/2H = 0.3$).

The heat transfer and skin friction coefficients are the two most important performance parameters concerning any heat transfer process. In the following text, we shall discuss about these two parameters.

In order to predict the heat transfer performance at the wall, the local Nusselt number may be defined as

$$Nu(x,Z) = \frac{hH}{k}$$

or

$$Nu(x,z) = h(T_w - T_b)\frac{\nu}{\alpha}\frac{1}{\rho c_p}\frac{1}{U_o(T_w - T_b)}\frac{U_o H}{\nu}$$

or

$$Nu(x,z) = \frac{q_w Pr\, Re}{\rho c_p (T_w - T_b) U_o}$$

or

$$Nu(x,z) = \frac{q_{w,n} Pr\, Re}{(\theta_w - \theta_b)} \qquad (30)$$

where

$$q_{w,n} = \frac{q_w}{\rho c_p (T_w - T_\infty) U_o}.$$

Finally, the spanwise average Nusselt number on the bottom fin surface may be expressed as

$$\overline{Nu}_{sl} = \frac{2}{B}\int_o^{B/2} Nu(x,z)\,\mathrm{d}z. \qquad (31)$$

Figure 15 shows the Nu_{sl} distribution on the bottom plate for the Reynolds number of 5000 and 15 000. In both the cases, the turbulent intensity is 10% at the inlet of the channel. Significant enhancement is observed for the cases with built-in delta winglets over the corresponding cases without any obstacle. For example, in the case of Reynolds number of 5000, the

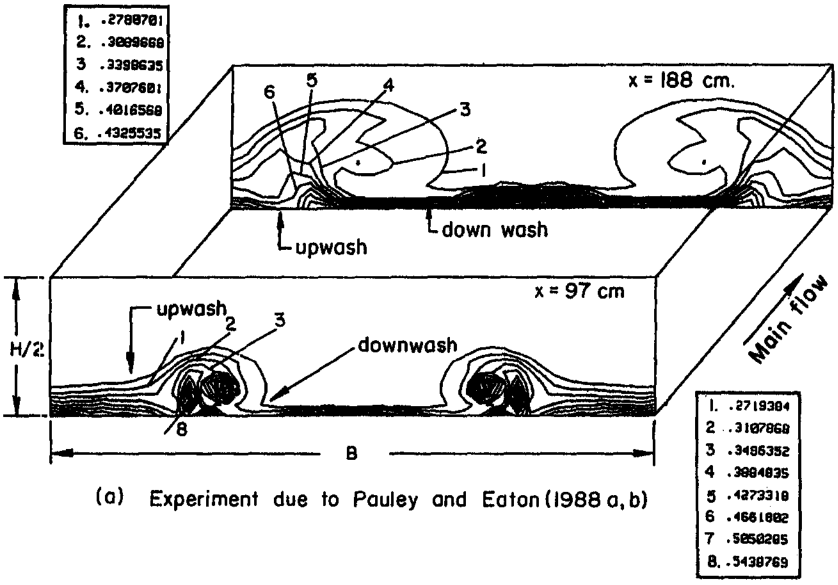

(a) Experiment due to Pauley and Eaton (1988 a, b)

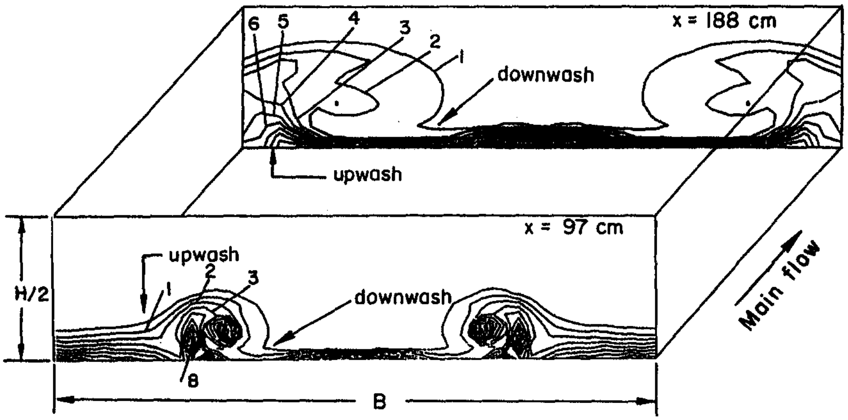

(b) Present computation

Fig. 12. Isolines for turbulent kinetic energy at different cross-sections for $Re_{H/2} = 67\,000$.

enhancement is about 16% at the exit of the channel. It may be worthwhile to mention here that the size of the winglets used in the study of turbulent flow is indeed smaller as compared to the size of the winglets used for the study in laminar flow. So, the enhancement in transport rate is not as high as laminar flows. The peak values are brought about just inboard of the vortex center where the lateral divergence is most pronounced (for both the cases, it is at $X = 2.5$ from the inlet).

Figure 16 shows that at the location of the peak, the boundary layer is thinned by the strong downflow and lateral outflow of boundary layer fluid. In the downstream the secondary velocities decay and vortices spread apart, causing a growth of the boundary layer.

The local skin friction coefficient at the bottom wall may be expressed as

$$C_f(x,z) = \frac{\tau_w}{\frac{1}{2}\rho U_o^2}$$

or

$$C_f(x,z) = 2\tau_{w,n}. \tag{32}$$

The spanwise average skin friction coefficient on the bottom wall is expressed as

$$C_{fsl} = \frac{2}{B}\int_o^{B/2} C_f(x,z)\,dz. \tag{33}$$

The distribution of spanwise average skin friction coefficient ($\bar{C}_{fsl} \times Re$) for two different Reynolds numbers is shown in Fig. 17. The increase in peak values of the average skin friction coefficients are 33 and 27% for the Reynolds numbers of 5000 and 15 000, respectively.

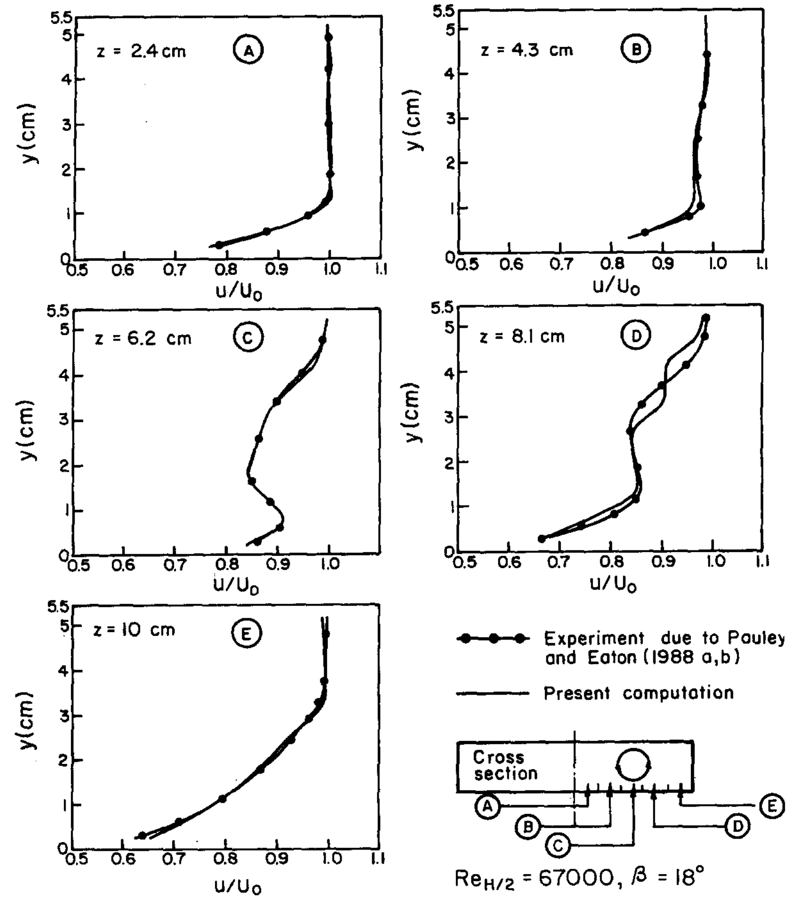

Fig. 13. Streamwise velocity profiles at axial station $x = 142$ cm for $Re_{H/2} = 67\,000$.

CONCLUDING REMARKS

A numerical model has been proposed to compute both the laminar and turbulent flows. The flow is described by the unsteady Reynolds averaged Navier–Stokes equations and the k–ε model of turbulence. To mimic the transport processes near the wall, the wall function treatment of Launder and Spalding [21] has been employed. The computed results are compared with the measurements of Pauley and Eaton [18, 19] and Eaton [20]. In general, the prediction is good, although slight discrepancies are observed in the prediction of turbulent kinetic energy at places where the boundary layer is severely distorted by the vortices. Finally some important predictions are made with respect to enhancement of heat transfer for various Reynolds numbers in the turbulent regime.

It is understood that the wall function approach used in turbulent flow computations greatly reduces the storage and computational time as compared to those associated with the low Reynolds-number near-wall models. However, it is also well-known that the wall-function approach is used on a rather simple intuition and it is not always consistent with complex physical picture near the wall. Over and above, in k–ε family of models the non-local property of turbulence is accounted for usually by one turbulent length scale that is dictated by a model equation which is derived on the basis of closure assumptions for most parts of the governing processes. Such models need several empirical coefficients and for obvious reasons such coefficients cannot be universal constants. Despite these limitations, many times k–ε types of eddy viscosity models have produced fairly acceptable results in predicting flows which have predominantly small-scale turbulence structures and which can be considered to be interpolates of basic experiments for which the coefficients have been determined.

Acknowledgements—The Authors acknowledge their gratitude to Professor John K. Eaton of Stanford University for providing with his experimental data tape. Sincere thanks are due to the reviewers for the valuable comments.

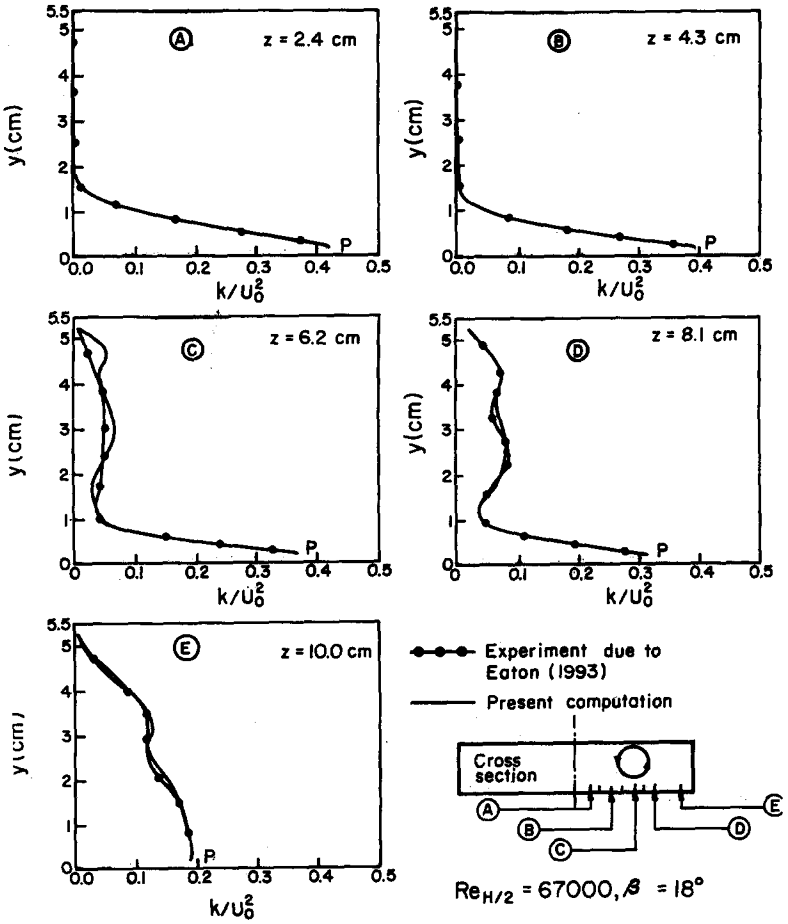

Fig. 14. Turbulent kinetic energy profiles at axial station $x = 188$ cm for $Re_{H/2} = 67\,000$.

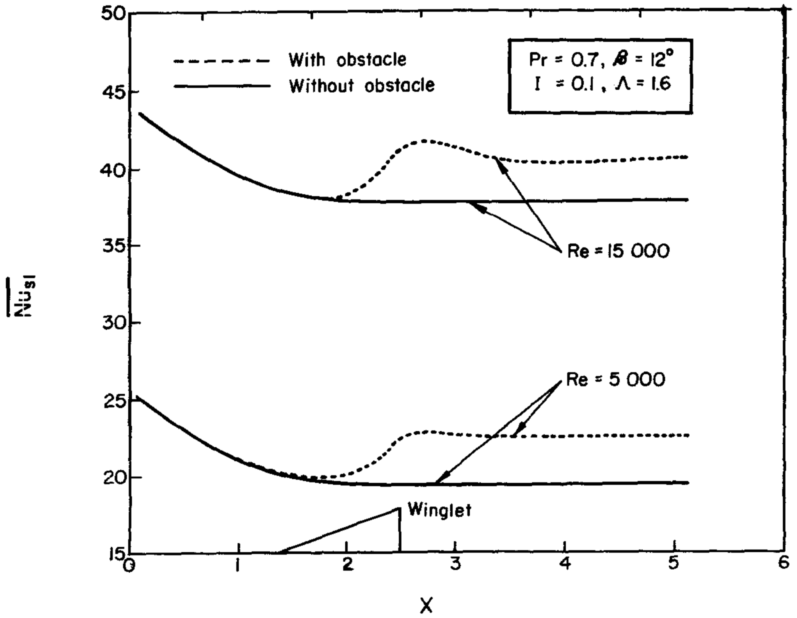

Fig. 15. Distribution of spanwise average Nusselt number on the bottom plate for different Reynolds numbers.

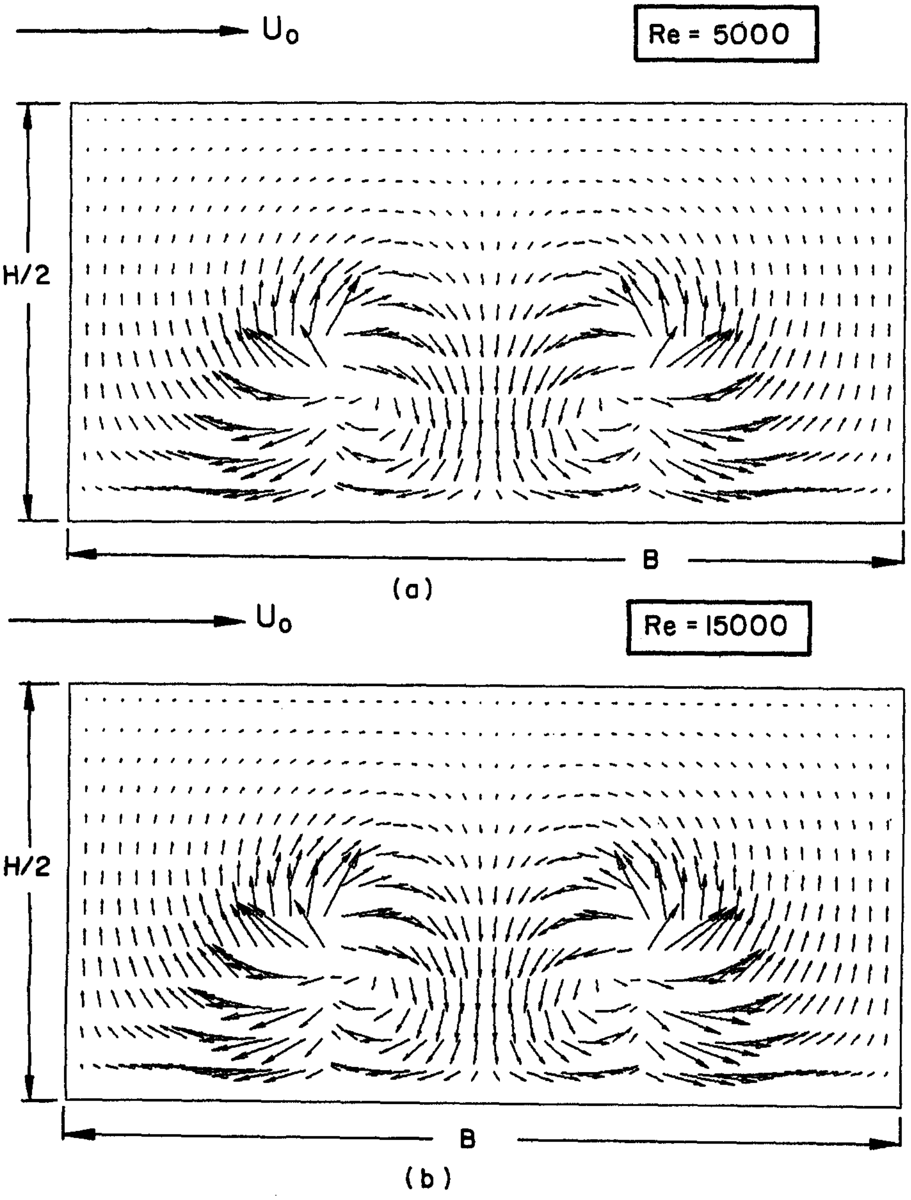

Fig. 16. Cross-stream velocity vectors at $X = 2.5$ from the inlet of the channel for two different Reynolds numbers.

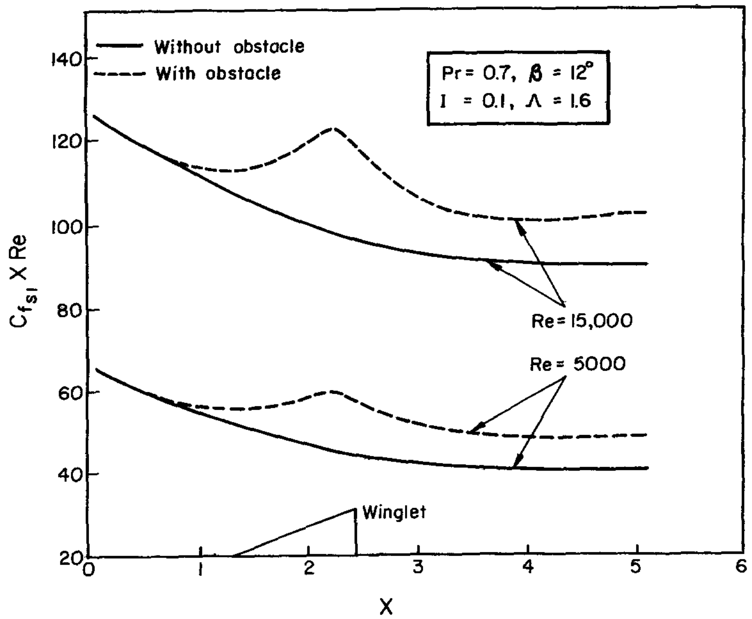

Fig. 17. Distribution of spanwise average skin friction coefficient on the bottom plate for different Reynolds numbers.

REFERENCES

1. R. L. Webb, Enhancement of single-phase convective heat transfer, *Handbook of Single Phase Convective Heat Transfer*. John Wiley, New York (1987).
2. A. E. Bergles, Enhancement of heat transfer, *Heat Transfer—1978, Proceedings of the Sixth International Heat Transfer Conference*, Vol. 6, pp. 89–168 (1978).
3. A. E. Bergles, Augmentation of heat transfer, *Heat Exchanger Design Handbook*, Vol. 2, pp. 2.5.11–1–12. Hemisphere Washington D.C. (1983).
4. A. E. Bergles, Techniques to augment heat transfer, *Handbook of Heat Transfer Applications*, pp. 31–80. McGraw-Hill, New York (1985).
5. F. J. Edwards and G. J. R. Alker, The improvement of forced convection surface heat transfer using surface protrusions in the form of (a) cubes and (b) vortex generators, *Proceedings of the Fifth International Heat Transfer Conference*, Tokyo, Vol. 2, pp. 2244–2248 (1974).
6. C. M. B. Russels, T. V. Jones and G. H. Lee, Heat transfer enhancement using vortex generators, *Proceedings of the Seventh International Heat Transfer Conference*, Munich, Vol. 3, pp. 283–288 (1982).
7. M. Fiebig, P. Kallweit and N. K. Mitra, Wing type vortex generators for heat transfer enhancement, *Proceedings of the Eighth International Heat Transfer Conference*, San Francisco, Vol. 6, pp. 2909–2913 (1986).
8. M. Fiebig, P. Kallweit, N. K. Mitra and S. Tiggelbeck, Heat transfer enhancement and drag by longitudinal vortex generators in channel flow, *Exp. Thermal Fluid Sci.* **4,** 103–114 (1991).
9. S. Tiggelbeck, N. K. Mitra and M. Fiebig, Flow structure and heat transfer in a channel with multiple longitudinal vortex-generators, *Exp. Thermal Fluid Sci.* **5,** 425–436 (1992).
10. M. Fiebig, U. Brockmeier, N. K. Mitra and T. Güntermann, Structure of velocity and temperature fields in laminar channel flows with longitudinal vortex generators, *Numer. Heat Transfer A* **15,** 281–302 (1989).
11. G. Biswas, and H. Chattopadhyay, Heat transfer in a channel with built-in wing-type vortex generators, *Int. J. Heat Mass Transfer* **35,** 803–814 (1992).
12. Y. Dong, Experimentelle Untersuchung der Wechselwirkung von Längswirbelerzeugern und Kreiszylindern in Bezug auf Wärmeubergang und Stromungsverlust, Doctoral Thesis, Ruhr University-Bochum, Germany (1989).
13. A. Valencia, Wärmeubergang und Druckverlust in Lamellen-Rohr-Wärmeubertragern mit Längswirbelerzugern, Doctoral Thesis, Ruhr University-Bochum, Germany (1992).
14. G. Biswas, N. K. Mitra, and M. Fiebig, Heat transfer enhancement in fin-tube heat exchangers by winglet-type vortex generators, *Int. J. Heat Mass Transfer* **37,** 283–291 (1994).
15. P. A. Eibeck and J. K. Eaton, Heat transfer effects of a longitudinal vortex embedded in a turbulent shear flow, *J. Heat Transfer* **109,** 16–24 (1987).
16. R. V. Westphal and R. D. Mehta, Interaction of an oscillating vortex with a turbulent boundary layer, *Proceedings of the AIAA 19th Fluid Dynamics and Laser Conference*, Hawaii, AIAA Paper no. 87, p. 1246 (1987).
17. J. X. Zhu, N. K. Mitra and M. Fiebig, Effects of longitudinal vortex generators on heat transfer and flow loss in turbulent channel flows, *Int. J. Heat Mass Transfer* **36,** 2339–2347 (1993).
18. W. R. Pauley and J. K. Eaton, The fluid dynamics and heat transfer effects of streamwise vortices embedded in a turbulent boundary layer, Rept MD-51, Thermosciences Division, Department of Mechanical Engineering, Stanford University, CA (1988).
19. W. R. Pauley and J. K. Eaton, Experimental study of the development of longitudinal vortex pairs embedded in a turbulent boundary layer, *AIAA J.* **26**(7), 816–823 (1988).
20. J. K. Eaton, Personal communication (a data tape of of well-documented experimental results was given to the authors) (1993).
21. B. E. Launder and D. B. Spalding, The numerical computation of turbulent flows, *Comput. Meth. Appl. Mech. Engng* **3,** 269–289 (1974).
22. S. Dutta and S. Acharya, Heat transfer and flow past a backstep with the nonlinear k–ε turbulence model and the modified k–ε turbulence model, *Numer. Heat Transfer A* **23,** 281–301 (1993).

23. F. H. Harlow and J. E. Welch, Numerical calculation of time-dependent viscous incompressible flow of fluid with free surface, *Phys. Fluids* **8**, 2182–2188 (1965).
24. C. W. Hirt and J. L. Cook, Calculating three-dimensional flows around structures and over rough terrain, *J. Comp. Phys.* **10**, 324–340 (1972).
25. C. W. Hirt, B. D. Nichols and N. C. Romero, SOLA—A numerical solution algorithm for transient fluid flows, Los Alamos Scientific Laboratory Report, LA-5652, (1975).
26. R. W. Davis and E. F. Moore, A numerical study of vortex shedding from rectangles, *J. Fluid Mech.* **116**, 475–506 (1982).
27. B. P. Leonard, A stable and accurate convective modelling procedure based on quadratic upstream interpolation, *Comput. Meth. Appl. Mech. Engng* **19**, 59–98 (1979).
28. T. Kawamura, H. Takami and K. Kuwahara, Computation of high Reynolds number flow around a circular cylinder with surface roughness, *Fluid Dyn. Res.* **1**, 145–162 (1986).
29. S. Shirayama, Construction of modified third-order upwind schemes for stretched meshes, *AIAA J.* **30**, 1237–1242 (1992).
30. U. Ghia, K. N. Ghia and C. T. Shin, High-resolutions for incompressible flow using the Navier–Stokes equations and a multigrid method, *J. Comp. Phys.* **48**, 387–411 (1982).
31. R. K. Shah and A. L. London, *Laminar Flow Forced Convection in Ducts*, *Advances in Heat Transfer*, Suppl. 1, pp. 169–176. Academic Press, New York (1978).
32. S. Kakac, R. K. Shah and A. E. Bergles, *Low Reynolds Number Flow Heat Exchangers*. Hemisphere, Washington, DC (1981).